Quaternary International 467 (2018) 251–263

Contents lists available at ScienceDirect

Quaternary International

journal homepage: www.elsevier.com/locate/quaint

Optical dating of Holocene sediments from the Yangtze River (Changjiang) Delta, China

Xiaomei Nian*, Weiguo Zhang, Zhanghua Wang, Qianli Sun, Jing Chen, Zhongyuan Chen

State Key Laboratory of Estuarine and Coastal Research, East China Normal University, Shanghai 200062, China

ARTICLE INFO

Article history:
Received 20 July 2017
Received in revised form
21 December 2017
Accepted 7 January 2018
Available online 11 January 2018

Keywords:
Optically stimulated luminescence (OSL)
Coarse silt-sized quartz (45–63 μm)
Fine sand-sized quartz (90–125 μm)
Holocene
Paleo-incised valley
Yangtze River (Changjiang) Delta

ABSTRACT

Establishing a reliable chronology is essential for understanding delta evolution, which is normally performed using radiocarbon (^{14}C) dating and the recently emerging technique of optically stimulated luminescence (OSL). The application of the latter one to the Holocene Yangtze River (Changjiang) Delta deposit is still quite limited. In this study, two 60.9-m-long cores were collected from Taizhou (TZ) and Nantong (NT) within the paleo-incised valley of the Yangtze River, and a total of seven and nine OSL samples were collected from the TZ and NT cores, respectively. In addition, ten accelerator mass spectrometry (AMS) ^{14}C ages of the TZ core were presented with eight AMS ^{14}C ages that were previously obtained from the NT core. The single-aliquot regenerative-dose (SAR) protocol was applied to coarse silt-sized (45–63 μm) and fine sand-sized (90–125 μm) quartz. The results showed that the grains in the 45–63 μm size fractions appeared to be better bleached than those in the 90–125 μm size fractions, and the detection of insufficiently bleached sediments is required in order to obtain accurate age estimates. The ages adopted for the samples range from 3 ka to 9 ka for the TZ core, and from 1 ka to 14 ka for the NT core, which were in general internally coherent within the limits of experimental errors and with respect to their stratigraphic order. The AMS ^{14}C age of the TZ core were significantly older than their OSL ages, while those from the NT core generally showed good agreement with their OSL ages. One should be cautious when using AMS ^{14}C to date deltatic deposits. Based on the OSL ages, two periods of rapid accumulation rates can be found in both cores, which are linked to the rapid sea level rise in early Holocene and migration of delta front facies in late Holocene. These investigations indicate that OSL technique is an effective method with which to date Holocene deltaic deposits, especially in coarse sedimentary layers where organic carbon material is sparse.

© 2018 Elsevier Ltd and INQUA. All rights reserved.

1. Introduction

The Yangtze River (Changjiang) Delta is one of the most densely populated mega-deltas in the world. Its Holocene deposits, which can reach thicknesses of up to 80 m in its incised paleo-river valley (Fig. 1), can be used to obtain high-resolution records of land-sea interaction history (Delta Research Group, 1978; Wang et al., 1981). Obtaining reliable geochronologic data is of paramount importance in investigations of deltaic palaeoenvironmental changes. To date, the dating of the Yangtze River Delta deposits has mainly been based on ^{14}C dating (e.g. Hori et al., 2001; Wang et al., 2012, 2013a; Xu et al., 2012; Feng et al., 2016). Based on a large number of ^{14}C age analyses, a general framework of sediment accumulation history in the incised-river valley and its implications for Holocene delta evolution have been well-established (e.g. Delta Research Group, 1978; Wang et al., 1981; Hori et al., 2001; Song et al., 2013). However, reworking of carbon material and carbon reservoir effect can yield inaccurate ages. It is common to observe age reversals in the delta stratigraphy (Stanley and Chen, 2000). In the study area, the Holocene stratigraphy in the incised-valley typically comprises a lower estuarine-marine facies and an upper delta facies (e.g. Li et al., 2000). The delta front facies often occurs in the upper 20 m of the stratigraphy, where sands represent the major sediment type and materials that are suitable for radiocarbon dating occur only sporadically. As a result, ^{14}C age analyses of the sandy delta front facies are very limited (e.g. cores of HQ98, JS98 and CM97 from Hori et al., 2001, 2002; JD01 from Song et al., 2013), leaving age 'blanks' in the studied cores, which impede the generation of high-resolution environmental records.

Optically stimulated luminescence (OSL) dating represents an

* Corresponding author.
E-mail address: xmnian@sklec.ecnu.edu.cn (X. Nian).

https://doi.org/10.1016/j.quaint.2018.01.011
1040-6182/© 2018 Elsevier Ltd and INQUA. All rights reserved.

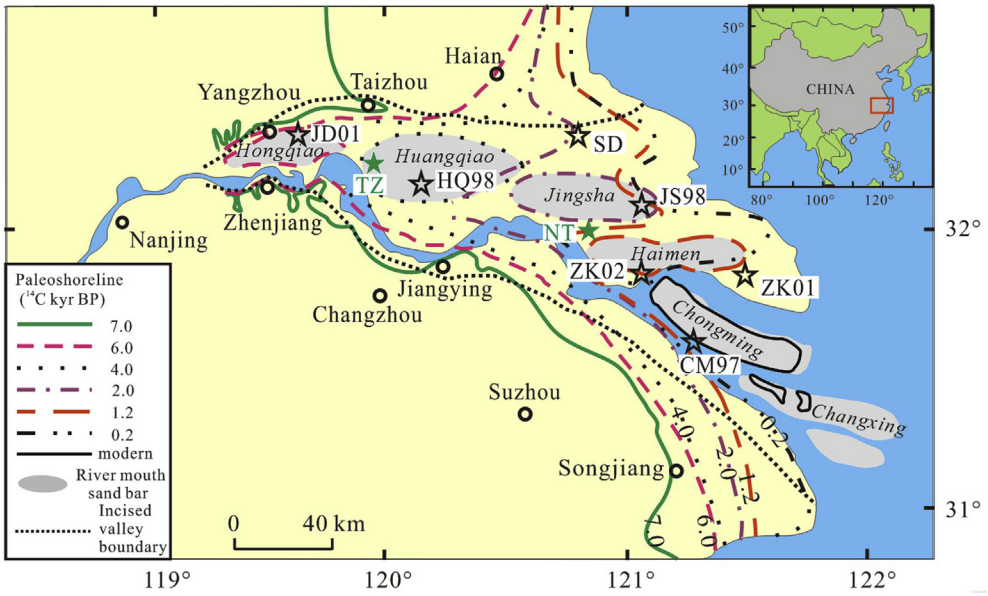

Fig. 1. Location map of the study area (modified from Song et al. (2013)), showing the geographic locations of the TZ and NT cores in this study. Also shows are published cores HQ98, JS98, CM97 (Hori et al., 2001, 2002), JD01 (Song et al., 2013), ZK01, ZK02 (Zhang et al., 2017), SD (Nian et al., 2018).

invaluable alternative technique that can be used to date coastal sediments (e.g. Roberts and Plater, 2007; Jacobs, 2008; Bateman, 2015; Oliver et al., 2015; Lamothe, 2016), and the precision and age ranges of these measurements have been improved recently. For example, this technique has been used to successfully date Holocene deposits in the Mississippi Delta (Shen and Mauz, 2012; Shen et al., 2015), the Mekong River Delta (Tamura et al., 2012), the Ganges-Brahmaputra-Meghna Delta (Chamberlain et al., 2017) and the Nakdong Delta (Kim et al., 2015). In recent years, the results of OSL chronologic analyses have also been reported for cores collected from the subaqueous Yangtze River Delta (Wang et al., 2013b; Sugisaki et al., 2015), the neighboring South Yellow Sea and East China Sea (Yi et al., 2014; Wang et al., 2015; Gao et al., 2016, 2017), and paleo-incised Yangtze River valley (Nian et al., 2018).

In this study, two 60.9-m-long cores were collected from Taizhou (TZ, 32°23.8317′N, 119°54.845′E, 4.72 m above sea level (asl)) and Nantong (NT, 32°3.9417′N, 120°51.4′E, 3.99 m asl) in the Yangtze River Delta in 2013. The OSL dating technique was applied to both the 45–63 μm and 90–125 μm quartz size fractions. Although it is difficult to perform ^{14}C dating in the study area, this method can still be used to produce a valuable chronological framework for the Holocene deposits. The OSL results were systematically compared with the obtained ^{14}C dating results in order to refine the chronology of the cores. The purpose of this study is to investigate the feasibility of using the OSL dating technique to determine the ages of Holocene deposits that exhibit significant variations in their particle size distributions. Suitable grain-size fractions and techniques for OSL dating are recommended, which may be applied to other studies performed in similar environmental settings.

2. Study area and samples

During the Last Glacial Maximum (LGM) of the Late Pleistocene, when the sea level was ca. 120 m below its present level, the present-day Yangtze River Delta region was incised, forming a river valley that was 70–80 m deep (Li et al., 2000). When postglacial transgression occurred, the Yangtze Estuary shifted landward in response to sea-level rise, and the apex of the delta retreated to the Zhenjiang and Yangzhou areas at approximately 8 ka (e.g. Song et al., 2013) (Fig. 1). Since then, the coastline has shifted seaward and the modern Yangtze River Delta was initiated when sea-level rise slowed down and huge amounts of sediment supply were deposited. It has been suggested that the Yangtze River Delta was formed through six subdelta stages, with each subdelta stage characterized by the formation of a river-mouth sand bar deposit in the upper 20 m of its stratigraphic sequence (Fig. 1; Wang et al., 1981; Li et al., 2000; Hori et al., 2001, 2002; Song et al., 2013). Based on the results of ^{14}C dating and archaeological evidence, the six stages of delta formation are defined as follows: the Hongqiao phase (7.5–6.0 ka or recently revised as 6.0–5.5 ka by Song et al., 2013), the Huangqiao phase (6.5–4.0 ka), the Jinsha phase (4.5–2.0 ka), the Haimen phase (2.5–1.2 ka), the Chongming phase (1.7–0.2 ka), and the Changxing phase (0.7 ka-present) (Delta Research Group, 1978; Song et al., 2013).

Cores TZ and NT (Fig. 1) are located in the sand bar deposits that were formed during the Huangqiao phase and between the Jinsha and the Haimen phases, respectively. Seven samples (TZ-1 to TZ-7) were collected from the TZ core and nine samples (NT-1 to NT-9) were collected from the NT core for OSL dating. Ten samples were collected from the TZ core for ^{14}C dating (Fig. 2). The lithology of the NT core and the results of its AMS ^{14}C age analyses were reported by Bai et al. (2016). According to lithology and the stratigraphic correlation with the well-established sedimentary facies of cores JD01 (Song et al., 2013), HQ98, JS98 (Hori et al., 2001, 2002), ZK01 and ZK02 (Zhang et al., 2017) from adjacent area (Fig. 1), five sedimentary units in ascending order were identified in the TZ core: estuary (TZ-U1), prodelta (TZ-U2), distributary channel (TZ-U3), delta front (TZ-U4), and delta plain (TZ-U5). Six sedimentary units were distinguished in the NT core: tidal river (NT-U1), estuary (NT-U2), tidal sand ridge (NT-U3), prodelta (NT-U4), delta front (NT-U5), and delta plain (NT-U6) (Fig. 2; Bai et al., 2016).

3. Methods

To select suitable grain-size intervals for OSL dating, the grain-size distributions of the sediments were measured using a

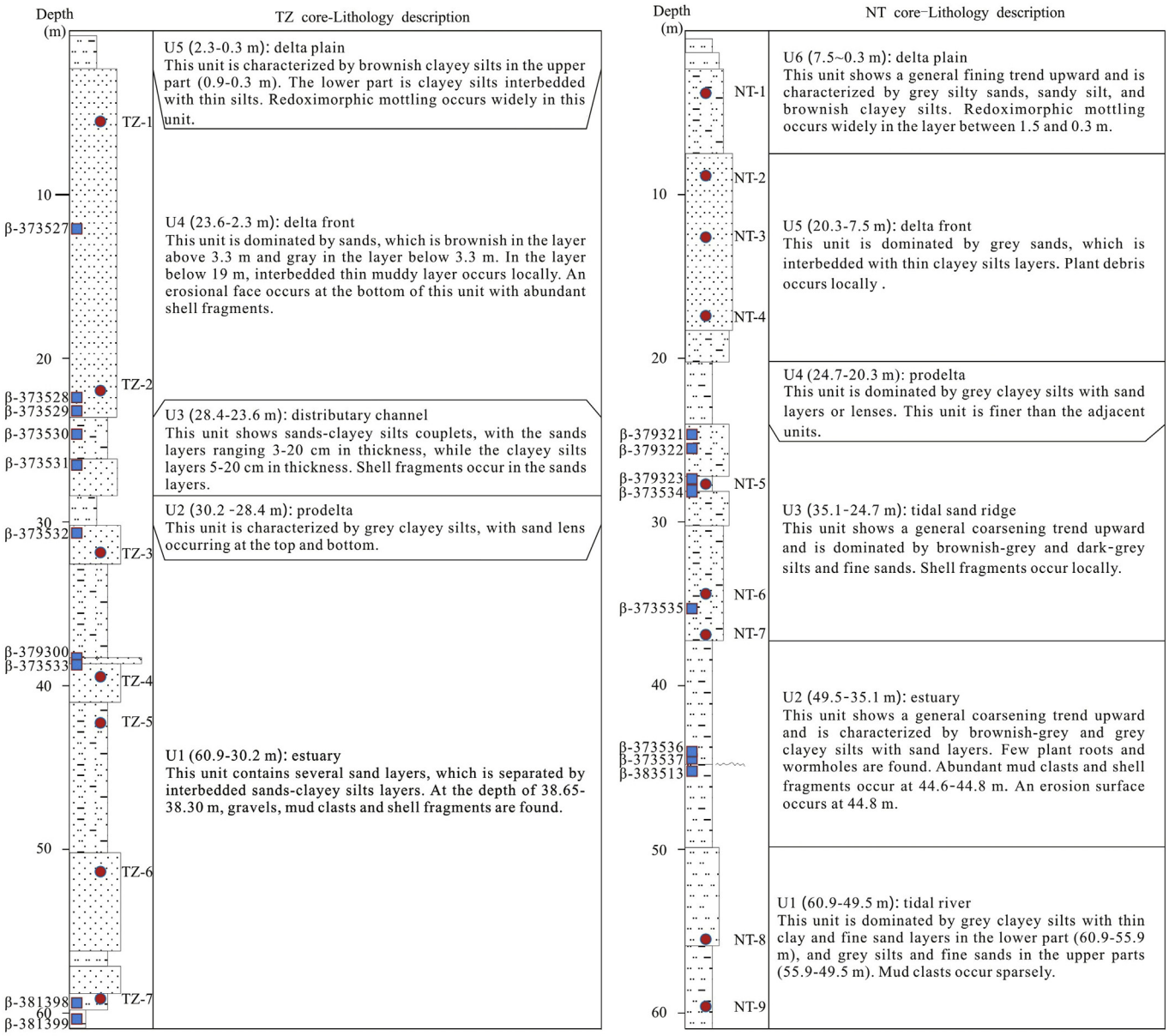

Fig. 2. Lithologic descriptions of the TZ and NT cores, showing the sampling locations of the samples used for OSL (solid circles) and ^{14}C (solid squares) dating.

Coulter LS13320 laser diffraction particle size analyzer. The Holocene sediments from the TZ and NT cores are characterized by grey and greenish-grey sandy silts, silty sands and fine to medium sands (Fig. S1). The two dominant grain-size fractions (45–63 μm and 90–125 μm) of the quartz extracted from these samples were used for OSL measurements.

All OSL sample preparations and measurements were performed under dim red light in order to avoid optical bleaching effects. The cores were split under subdued red light, the samples were removed from the sediment core in metal tubes and kept in a refrigerator to ensure limited evaporation. After removing the outer layers of the samples, the inner cores of the samples were treated with 30% hydrogen peroxide (H_2O_2) and 10% hydrochloric acid (HCl) in order to remove organic matter and carbonates, respectively. After treatment with H_2O_2 and HCl, the raw sediment samples were then rinsed and wet-sieved to retain the grain-size fractions of 45–63 μm and 90–125 μm. Coarse silt-sized and fine sand-sized polymineral grains were then etched using 30% fluorosilicic acid for 3–4 days and 40% hydrofluoric acid for 40 min, respectively, in order to obtain quartz grains. The purity of the quartz separates was determined based on their OSL-IR (infrared) depletion ratios (>0.9) (Duller, 2003) and thermoluminescence (TL) measurements (with a TL peak of 110 °C) (Li et al., 2002).

All luminescence measurements, beta irradiation and preheat treatments were carried out using an automated Risø-TL/OSL DA-20 DASH reader equipped with a $^{90}Sr/^{90}Y$ beta source (Bøtter-Jensen et al., 2003) and an ET EMD-9107 photomultiplier tube. A 470 nm blue light set at 90% of its full power of 97 mW cm^{-2} and a 7.5 mm Hoya U-340 filter were used for the quartz OSL measurements. Neutron activation analysis (NAA) was used to determine the uranium, thorium and potassium contents of these samples (Table 1). An alpha efficiency factor (a-value) of 0.04 ± 0.02 was used for the 45–63 μm quartz grains (Rees-Jones, 1995). The attenuation factors proposed by Brennan et al. (1991) and Guerin et al. (2012) were used to calculate the alpha and beta dose rates, respectively. The water contents (weight of water/weight of dry

Table 1
Summary of dosimetry of the samples from the TZ and NT cores.

Field No.	U (ppm)	Th (ppm)	K (%)	Depth (m)	Water (%)	Grain size (μm)	Environmental dose rate (Gy/ka)				
							Alpha	Beta	Gamma	Cosmic	Total
TZ-1	1.43 ± 0.07	9.42 ± 0.27	1.67 ± 0.06	5.28–5.40	30 ± 5	45–63	0.09± 0.04	1.24 ± 0.07	0.76 ± 0.04	0.106 ± 0.011	2.20 ± 0.08
						90–125	–	1.19 ± 0.06			2.05 ± 0.07
TZ-2	1.43 ± 0.07	10.5 ± 0.29	1.47 ± 0.05	21.58–21.70	31 ± 5	45–63	0.10 ± 0.04	1.14 ± 0.06	0.75 ± 0.04	0.028 ± 0.003	2.02 ± 0.08
						90–125	–	1.09 ± 0.06			1.87 ± 0.07
TZ-3	1.08 ± 0.06	6.69 ± 0.23	1.79 ± 0.06	32.08–32.20	34 ± 5	45–63	0.06 ± 0.03	1.18 ± 0.06	0.63 ± 0.03	0.016 ± 0.002	1.89 ± 0.07
						90–125	–	1.14 ± 0.06			1.79 ± 0.07
TZ-4	0.63 ± 0.04	3.99 ± 0.15	2.06 ± 0.06	39.08–39.20	34 ± 5	45–63	0.04 ± 0.02	1.24 ± 0.07	0.55 ± 0.03	0.011 ± 0.001	1.84 ± 0.07
						90–125	–	1.20 ± 0.06			1.76 ± 0.07
TZ-5	1.49 ± 0.07	8.74 ± 0.26	1.75 ± 0.06	42.08–42.20	29 ± 5	45–63	0.09 ± 0.04	1.29 ± 0.07	0.76 ± 0.04	0.010 ± 0.001	2.15 ± 0.09
						90–125	–	1.24 ± 0.07			2.01 ± 0.08
TZ-6	1.60 ± 0.07	9.38 ± 0.27	1.73 ± 0.06	51.08–51.20	31 ± 5	45–63	0.09 ± 0.04	1.28 ± 0.07	0.77 ± 0.04	0.007 ± 0.001	2.16 ± 0.09
						90–125	–	1.23 ± 0.06			2.01 ± 0.07
TZ-7	1.94 ± 0.08	11.4 ± 0.32	1.76 ± 0.06	58.78–58.90	33 ± 5	45–63	0.10 ± 0.04	1.31 ± 0.07	0.81 ± 0.04	0.006 ± 0.001	2.23 ± 0.09
						90–125	–	1.25 ± 0.07			2.07 ± 0.08
NT-1	3.01 ± 0.11	11.6 ± 0.32	1.64 ± 0.05	3.78–3.90	31 ± 5	45–63	0.14 ± 0.05	1.41 ± 0.07	0.95 ± 0.04	0.125 ± 0.012	2.63 ± 0.01
						90–125	–	1.34 ± 0.07			2.42 ± 0.08
NT-2	1.51 ± 0.07	8.94 ± 0.27	1.77 ± 0.06	8.78–8.90	31 ± 5	45–63	0.09 ± 0.04	1.29 ± 0.07	0.76 ± 0.04	0.074 ± 0.007	2.21 ± 0.08
						90–125	–	1.23 ± 0.07			2.07 ± 0.08
NT-3	1.28 ± 0.06	8.88 ± 0.27	1.63 ± 0.05	12.78–12.90	33 ± 5	45–63	0.08 ± 0.03	1.16 ± 0.06	0.70 ± 0.03	0.052 ± 0.005	2.00 ± 0.08
						90–125	–	1.12 ± 0.06			1.87 ± 0.07
NT-4	1.42 ± 0.07	6.90 ± 0.22	1.84 ± 0.06	17.78–17.90	35 ± 5	45–63	0.07 ± 0.03	1.24 ± 0.06	0.67 ± 0.03	0.036 ± 0.004	2.01 ± 0.08
						90–125	–	1.19 ± 0.06			1.89 ± 0.07
NT-5	1.31 ± 0.07	7.85 ± 0.24	1.81 ± 0.06	27.78–27.90	34 ± 5	45–63	0.08 ± 0.03	1.24 ± 0.06	0.69 ± 0.03	0.019 ± 0.002	2.02 ± 0.08
						90–125	–	1.19 ± 0.06			1.90 ± 0.07
NT-6	1.79 ± 0.08	11.6 ± 0.32	1.67 ± 0.06	33.78–33.90	39 ± 5	45–63	0.10 ± 0.04	1.22 ± 0.06	0.80 ± 0.04	0.014 ± 0.001	2.14 ± 0.08
						90–125	–	1.16 ± 0.06			1.98 ± 0.07
NT-7	1.22 ± 0.06	7.72 ± 0.25	1.74 ± 0.06	36.78–36.90	33 ± 5	45–63	0.07 ± 0.03	1.20 ± 0.06	0.67 ± 0.03	0.013 ± 0.001	1.96 ± 0.08
						90–125	–	1.15 ± 0.06			1.84 ± 0.07
NT-8	1.25 ± 0.06	6.96 ± 0.23	1.65 ± 0.05	55.78–55.90	33 ± 5	45–63	0.07 ± 0.03	1.14 ± 0.06	0.64 ± 0.03	0.006 ± 0.001	1.85 ± 0.07
						90–125	–	1.09 ± 0.06			1.73 ± 0.07
NT-9	2.27 ± 0.09	10.7 ± 0.30	1.62 ± 0.05	59.78–59.90	34 ± 5	45–63	0.11 ± 0.04	1.28 ± 0.06	0.84 ± 0.04	0.005 ± 0.001	2.23 ± 0.09
						90–125	–	1.21 ± 0.06			2.05 ± 0.07

sediment) of these samples were measured in the laboratory and each value was assigned an uncertainty of ±5% in the age calculations. The dose rates and final ages were calculated using the Dose Rate and Age Calculator ('DRAC') (Durcan et al., 2015).

The single-aliquot regenerative-dose (SAR) protocol (Murray and Wintle, 2000) was applied to aliquots of grains that were 2 mm in diameter in order to determine the equivalent dose (D_e) of the samples. The aliquots were stimulated at 125 °C, and preheat temperatures of 180 °C (for samples from the TZ core) or 200 °C (for samples from the NT core) for 10 s, as well as a cut heat temperature of 160 °C for 0 s (Table S1), were used on the basis of preheat plateau tests. A blue light stimulation was used at 280 °C for 40 s at the end of each SAR cycle to remove the remaining signals. The initial 0.4 s integral of the OSL decay curve, after subtracting an early background integral of 0.4–1.4 s (Ballarini et al., 2007), was used to calculate the D_e to ensure that the signals were dominated by the fast component. The growth curves were fitted using single saturating exponential functions. All OSL ages are reported relative to 2013 CE.

The AMS ^{14}C samples consist of shells and plant fragments. Eight samples of shells and two samples of plant were selected from the TZ core, and seven shell samples and one plant fragment from the NT core (Bai et al., 2016). All samples were dated using AMS at the Beta Analytic Radiocarbon Dating Laboratory (Florida, USA). All conventional ages were calibrated using the CALIB REV 7.1 program and the IntCal13 Marine13 (shell) and IntCal13 (plant fragment, peat) calibration curves, which were used for marine and terrestrial materials, respectively (Reimer et al., 2013). A regional marine reservoir correction (ΔR) of −1 ± 143 years was utilized for the analyses of shell samples (Southon et al., 2002; Kong et al., 2005; Yoneda et al., 2007). After undergoing calibrations, all ^{14}C ages were converted to ka relative to 2013 CE in order to directly compare them with OSL ages.

4. Results

4.1. Routine tests of the SAR protocol

Sensitivity changes were checked using repeated measurements of a fixed regenerative dose and test dose during the SAR protocol (Murray and Wintle, 2000). The plots of regenerated L_x vs. the luminescence intensity of the test dose T_x show a straight line passing through the origin (Fig. S2), thus indicating that the sensitivity correction in the SAR measurement procedure works well.

To test the dependence of the D_e values on the preheat temperature, preheat plateau tests were performed on the 45–63 μm/90–125 μm quartz size fractions of samples TZ-5, NT-1 and NT-4 using 10 s preheats at 160, 180, 200, 220, 240, 260, 280 and 300 °C, with a cut heat temperature of 160 °C, for the SAR protocol. As shown in Fig. 3, together with the corresponding recycling ratios and recuperation values, preheat plateaus are evident between 160 and 220 °C for the 45–63 μm/90–125 μm quartz size fractions from sample TZ-5 and between 200 and 260 °C for both the 45–63 μm and 90–125 μm size fractions of the quartz extracted from samples NT-1 and NT-4 (Fig. 3). Recuperation values exhibit a systematic trend, but nevertheless fall within 3% for the 45–63 μm/90–125 μm quartz size fractions of sample TZ-5 and the 45–63 μm quartz size fractions of sample NT-1 (Fig. 3a, b, c); there is also a significant increase in the values of the 90–125 μm quartz size fractions of sample NT-4 during its high-temperature preheating up to 280 °C (Fig. 3d). The recycling ratios of these samples were within 10% of

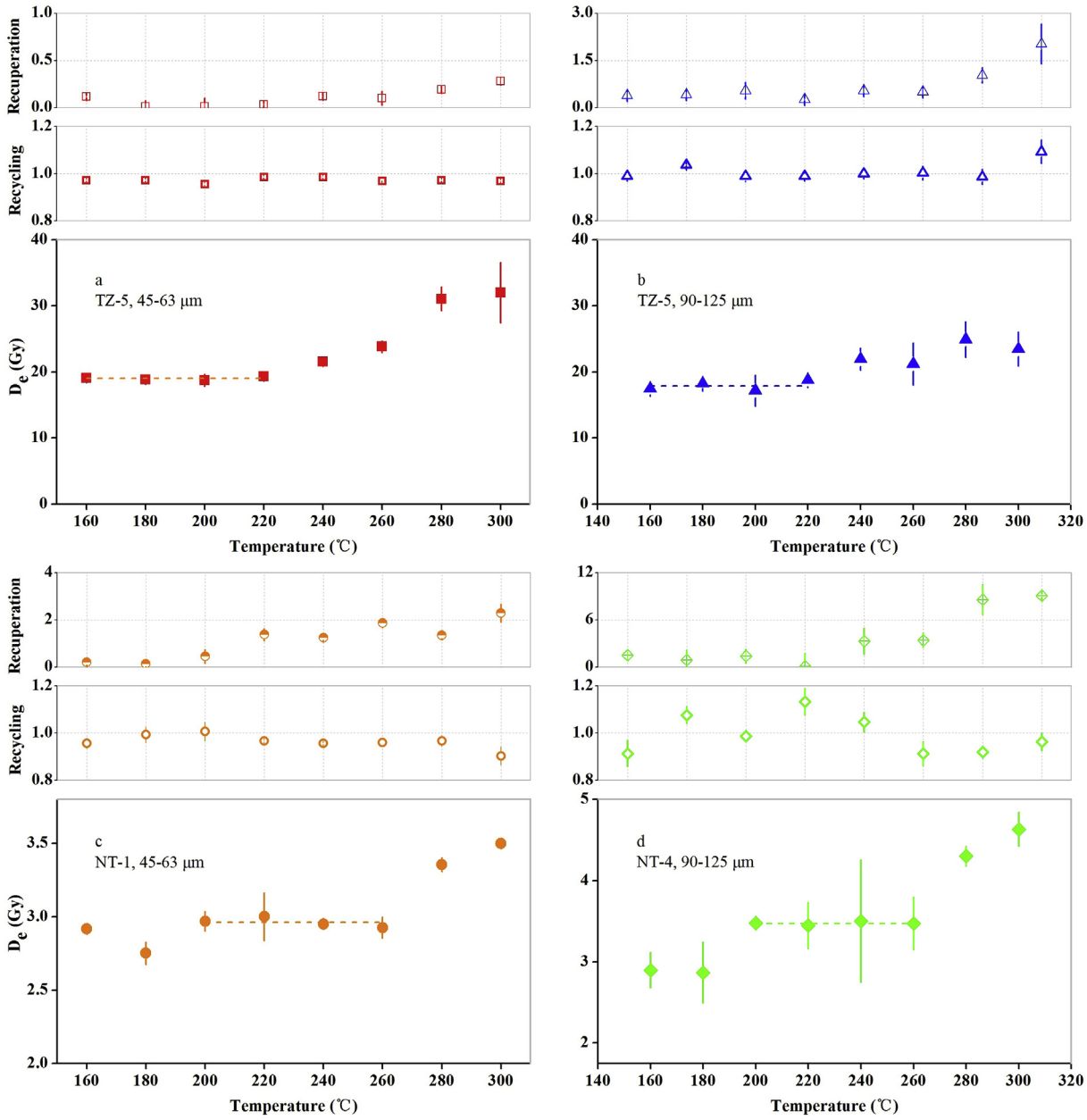

Fig. 3. Preheat plateau for samples from the TZ and NT cores and their corresponding recycling ratios and recuperation values (from at least 3 aliquots at each temperature). The dashed lines represent the mean D_e values between 160 and 220 °C for the samples from the TZ core and the mean D_e values between 200 and 260 °C for the samples from the NT core. Red square symbols (a): 45–63 μm quartz size fractions of sample TZ-5; blue triangle symbols (b): 90–125 μm quartz size fractions of sample TZ-5; orange circle symbols (c): 45–63 μm quartz size fractions of sample NT-1; green diamond symbols (d): 90–125 μm quartz size fractions of sample NT-4. (For interpretation of the references to color in this figure legend, the reader is referred to the Web version of this article.)

unity. Preheat temperatures of 180 °C for the TZ samples and 200 °C for the NT samples, as well as a cut heat temperature of 160 °C, were selected for D_e determinations, based on the results of these preheat plateau tests.

Dose recovery tests (Murray and Wintle, 2003) were carried out on different grain-size fractions of samples TZ-5, NT-1 and NT-4 using a preheat of 10 s at 180/200 °C and a cut heat of 0 s at 160 °C. The samples were bleached using a Hönle solar simulator (SOL2) for 1 h; then, known laboratory doses were applied and measured using the fixed test dose. The laboratory doses were chosen to approximate equivalent paleodoses. The dose recovery ratios (recovered/given dose) are within 10% of unity, which is acceptable (Table S2). The above results indicate that the SAR protocols were suitable for the determination of D_e in these samples.

4.2. OSL age estimates

Fig. 4 presents the representative decay curves and dose-response curves of the 45–63 μm/90–125 μm quartz size fractions from samples TZ-5, NT-1 and NT-4. We calculated the D_e values of all the samples by the central age model (CAM) and the minimum age model (MAM) (Galbraith et al., 1999) (Table 2). The adopted model ages selected at the single-aliquot analytical scale are based on the statistical procedure of Arnold et al. (2007), and are shown in bold in Table 2. The CAM and MAM yielded identical

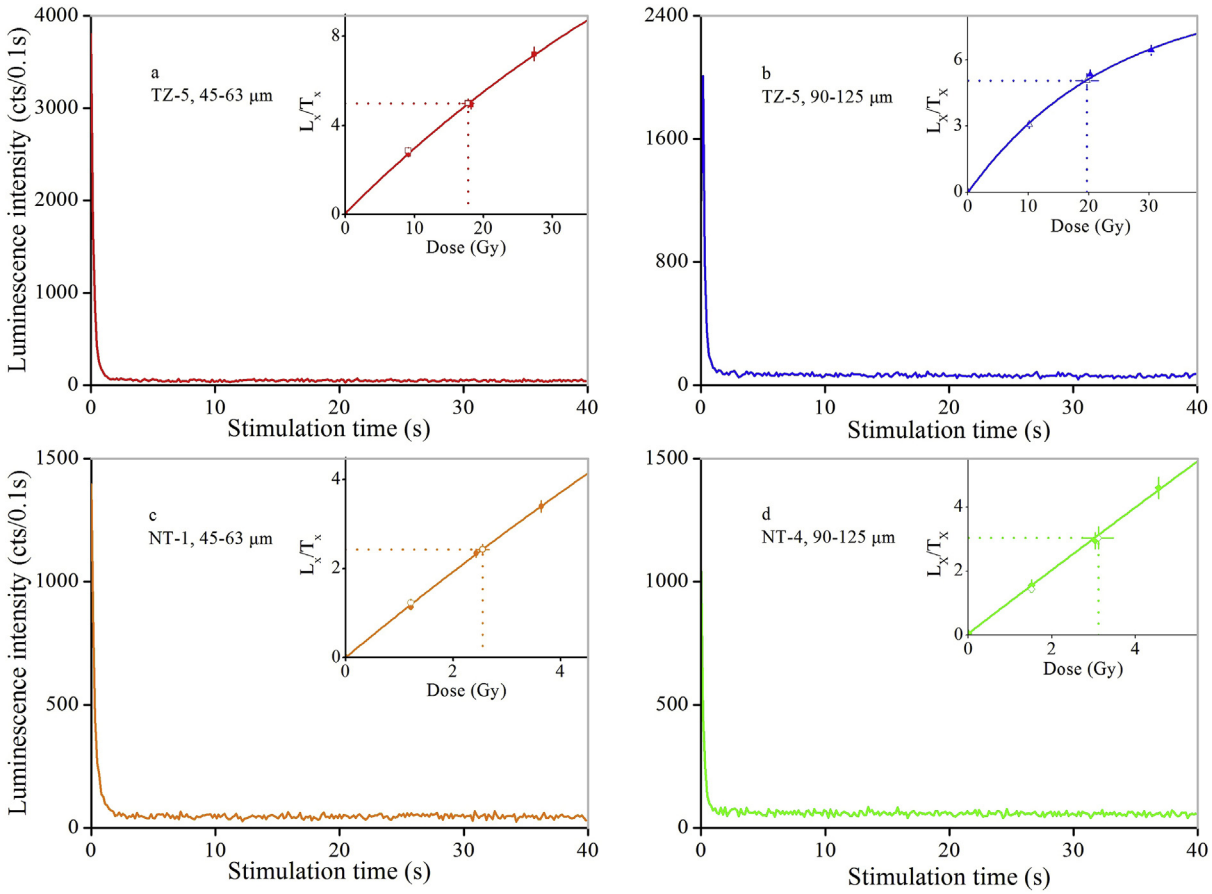

Fig. 4. Natural quartz OSL decay curves of different samples from the TZ and NT cores, using the analyses of 45–63 μm and 90–125 μm quartz size fractions; the corresponding dose-response curves, constructed using the SAR protocol, are shown in inset figures. The corrected OSL signal (L_x/T_x) represents the sensitivity-corrected OSL signal to the test dose. Different colors of symbols and lines represent different grains, and the legends are the same as that in Fig. 3. (For interpretation of the references to color in this figure legend, the reader is referred to the Web version of this article.)

D_e values for these samples within the uncertainty associated with this dating method, with an over-dispersion (OD) of less than 17% (with an average value of 12 ± 2%) for the 90–125 μm quartz size fractions and an OD of less than 11% (with an average value of 8 ± 1%) for the 45–63 μm quartz size fractions, thus suggesting that the OD of well-bleached samples in the Yangtze Delta is approximately 10%. In addition, the OD values of the recovered doses from the dose recovery experiment ranged from 7 ± 1% to 11 ± 3% for samples TZ-1, NT-1 and NT-4 (Table S2). These grains were bleached in a Hönle SOL2 daylight simulator for 1 h and are therefore considered well-bleached. The heterogeneity in the natural beta dose rate likely accounts for some of this OD (Arnold and Roberts, 2009); thus, the MAM, with a sigma b value of 0.1, was used to calculate the D_e values. This OD value is consistent with that previously reported in Mississippi Delta sediments (Shen et al., 2015). In the following discussion, the D_e values and OSL ages obtained using the suggested age models are presented.

Example distributions of the D_e values for samples TZ-3, TZ-5, NT-1, NT-4 and NT-5 are presented as histograms and radial plots in Fig. 5 (45–63 μm) and Fig. 6 (90–125 μm). Histograms and radial plots for the D_e values of the other samples are plotted in Fig. S3 (TZ, 45–63 μm), Fig. S4 (NT, 45–63 μm), Fig. S5 (TZ, 90–125 μm) and Fig. S6 (NT, 90–125 μm). The OSL ages of the TZ core ranged from 3.20 ± 0.14 ka to 8.48 ± 0.35 ka for the 45–63 μm quartz size fractions and from 3.37 ± 0.13 ka to 9.54 ± 0.54 ka for the 90–125 μm quartz size fractions (Table 2). The OSL ages of the NT core ranged from 1.07 ± 0.05 ka to 14.15 ± 0.71 ka for the 45–63 μm quartz size fractions and from 1.48 ± 0.16 ka to 12.47 ± 1.26ka for the 90–125 μm quartz size fractions (Table 2).

4.3. ^{14}C age determinations

All radiocarbon ages are summarized in Table 3. The ^{14}C ages of the eight shell samples collected from the TZ core ranged from 4.34 ± 0.41 ka to 11.07 ± 0.41 ka between depths of 12 m and 38.57 m, whereas the two plant fragment samples yielded ages of 8.97 ± 0.12 ka and 9.85 ± 0.13 ka at depths of 59.84 m and 60.2 m, respectively. The AMS ^{14}C ages of seven shell samples ranged from 3.64 ± 0.37 ka to 9.37 ± 0.35 ka between depths of 24.7 m and 44.8 m, and one plant fragment sample yielded an age of 10.71 ± 0.08 ka at depth of 45.62 m (Bai et al., 2016).

5. Discussion

5.1. Comparison of OSL ages from different grain size

In the TZ core, the ages of the 90–125 μm quartz size fractions were indistinguishable from those of the 45–63 μm quartz size fractions, except in samples TZ-3 and TZ-5 (which come from unit TZ-U1 and comprise tide-influenced estuary facies). In these two samples, the ages of their 90–125 μm quartz size fractions were significantly older than those of their 45–63 μm quartz size fractions, as seen in Table 2 and Fig. 7. Except for the age of the 45–63 μm quartz size fractions of sample TZ-5, which was obtained

Table 2
The ages of the samples with 45–63 μm and 90–125 μm quartz SAR protocol.

FieldNo.	45-63 μm quartz						90-125 μm quartz						
	Number of aliquots[a]	Over-dispersion	CAM-De (Gy)	CAM-Age (ka)	MAM-De (Gy)	MAM-Age[b] (ka)	Model selections	Number of aliquots	Over-dispersion	CAM-De (Gy)	CAM-Age (ka)	MAM-De (Gy)	MAM-Age (ka)	Model selections
TZ-1	31	0.05 ± 0.02	7.03 ± 0.11	3.20 ± 0.13	**7.03 ± 0.16**	**3.20 ± 0.14**	MAM	42	0.08 ± 0.02	**6.91 ± 0.12**	**3.37 ± 0.13**	6.89 ± 0.14	3.36 ± 0.14	CAM
TZ-2	29	0.16 ± 0.03	8.03 ± 0.29	3.98 ± 0.21	**7.77 ± 0.51**	**3.85 ± 0.30**	MAM	36	0.16 ± 0.03	8.15 ± 0.26	4.36 ± 0.21	**7.03 ± 0.46**	**3.76 ± 0.28**	MAM
TZ-3	29	0.29 ± 0.05	13.18 ± 0.79	6.96 ± 0.50	**8.39 ± 0.72**	**4.43 ± 0.42**	MAM	33	0.24 ± 0.04	13.99 ± 0.65	7.84 ± 0.47	**10.83 ± 0.93**	**6.07 ± 0.57**	MAM
TZ-4	–	–	–	–	–	–	–	39	0.21 ± 0.03	17.79 ± 0.63	10.1 ± 0.53	**14.01 ± 0.95**	**7.95 ± 0.62**	MAM
TZ-5	36	0.04 ± 0.02	**18.24 ± 0.24**	**8.48 ± 0.35**	18.34 ± 0.38	8.53 ± 0.38	CAM	47	0.10 ± 0.02	19.37 ± 0.35	9.65 ± 0.40	**19.16 ± 0.8**	**9.54 ± 0.54**	MAM
TZ-6	26	0.02 ± 0.05	17.83 ± 0.38	8.27 ± 0.37	**17.90 ± 0.79**	**8.30 ± 0.49**	MAM	32	0.07 ± 0.02	**17.96 ± 0.32**	**8.95 ± 0.37**	17.95 ± 0.40	8.95 ± 0.39	CAM
TZ-7	31	0.08 ± 0.01	**18.46 ± 0.31**	**8.29 ± 0.35**	18.49 ± 0.38	8.31 ± 0.37	CAM	28	0.17 ± 0.03	**18.26 ± 0.65**	**8.84 ± 0.45**	15.74 ± 1.17	7.62 ± 0.63	CAM
NT-1	29	0.07 ± 0.01	**2.8 ± 0.05**	**1.07 ± 0.05**	2.79 ± 0.06	1.06 ± 0.05	CAM	–	–	–	–	–	–	–
NT-2	28	0.06 ± 0.02	**2.51 ± 0.05**	**1.14 ± 0.05**	2.52 ± 0.06	1.14 ± 0.05	CAM	–	–	–	–	–	–	–
NT-3	29	0.06 ± 0.03	**2.55 ± 0.06**	**1.28 ± 0.06**	2.56 ± 0.12	1.28 ± 0.08	CAM	23	0.33 ± 0.06	3.83 ± 0.26	2.05 ± 0.16	**2.77 ± 0.29**	**1.48 ± 0.16**	MAM
NT-4	32	0.08 ± 0.02	2.82 ± 0.05	1.40 ± 0.06	**2.82 ± 0.10**	**1.40 ± 0.07**	MAM	30	0.12 ± 0.03	3.09 ± 0.09	1.63 ± 0.08	**3.08 ± 0.18**	**1.63 ± 0.11**	MAM
NT-5	29	0.11 ± 0.02	**15.03 ± 0.36**	**7.43 ± 0.33**	14.42 ± 0.66	7.12 ± 0.42	CAM	24	0.46 ± 0.07	20.82 ± 2.01	10.96 ± 1.13	**12.3 ± 2.16**	**6.48 ± 1.16**	MAM
NT-6	30	0.10 ± 0.02	17.37 ± 0.39	8.12 ± 0.36	**17.05 ± 0.80**	**7.97 ± 0.48**	MAM	22	0.15 ± 0.03	17.83 ± 0.69	9.01 ± 0.47	**16.62 ± 1.27**	**8.40 ± 0.70**	MAM
NT-7	28	0.09 ± 0.02	**17.67 ± 0.39**	**9.02 ± 0.40**	17.67 ± 0.41	9.02 ± 0.41	CAM	26	0.28 ± 0.04	23.58 ± 1.38	12.83 ± 0.89	**17.62 ± 1.58**	**9.59 ± 0.93**	MAM
NT-8	28	0.09 ± 0.02	26.17 ± 0.60	14.15 ± 0.64	**26.17 ± 0.82**	**14.15 ± 0.71**	MAM	27	0.25 ± 0.04	27.07 ± 1.50	15.61 ± 1.05	**21.62 ± 2.02**	**12.47 ± 1.26**	MAM
NT-9[c]	–	–	–	–	–	–	–	27	0.15 ± 0.03	30.53 ± 1.06	14.86 ± 0.73	**23.79 ± 1.83**	**11.58 ± 0.98**	CAM

[a] "–" Note: means the samples without enough 45–63 or 90–125 μm quartz grains to allow OSL measurement.
[b] The age model used to calculate the final OSL ages for the samples are shown in bold.
[c] The MAM age of sample NT-9 is adopted in comparison to the sea-level curve and its genetic depositional environment.

using the CAM, the ages of all samples (i.e. three of four) were calculated using the MAM; thus, the anomalous ages of the 90–125 μm quartz size fractions of samples TZ-3 and TZ-5 are probably due to their insufficient bleaching. These results suggest that the 45–63 μm quartz size fractions of these samples were generally better bleached than their 90–125 μm quartz size fractions. Issues with partial bleaching often occur in water-transported sediment grains due to their insufficient exposure to sunlight (e.g. Wallinga, 2002). Different grain sizes have different transport mechanisms. Coarse silt-sized sediments are likely transported in suspended loads, which have multiple opportunities to undergo bleaching during transportation and are thus completely bleached. The incomplete bleaching of fine sand-sized grains may be caused by bedload transport in turbid environments. As a result of limited light exposure within clear or turbid water, these grains can yield ages that overestimate their true depositional ages (Nian et al., 2018). The ages of samples TZ-5-7, which were collected from unit TZ-U1 (i.e. tide-influenced estuary facies) at depths between 42 m and 59 m, are relatively constant at 8.5 ka for both the 45–63 μm and 90–125 μm quartz size fractions. These results most likely indicate that a period of rapid deposition occurred. In the NT core, there is no significant difference between the ages of the 45–63 μm and 90–125 μm quartz size fractions, within experimental error; their OSL ages generally increase down-section and do not display any significant age reversals. In the NT core, The OSL ages obtained for these two grain-size fractions are in good agreement with each other and are also consistent with their stratigraphic order, as they increase with depth (Fig. 7).

The OSL ages of some typical fluvio-deltaic deposits in the Mississippi Delta, the Mekong River Delta, the Nakdong Delta, the Yangtze River Delta, and the Yellow River Delta are shown in Table 4. Nearly all these OSL ages show internal coherence and good agreement with their independently determined ages within the range of uncertainty; these ages are independent of grain size in all sites, except for the inner shelf of the East China Sea (Wang et al., 2015) and the paleo-incised Yangtze valley (Nian et al., 2018 and this study). Wang et al. (2015) used an independent age control to determine that one of the three coarse-grained quartz samples yielded an overestimated age due to the effects of partial bleaching; they also determined that fine-grained quartz appeared to yield the most reliable ages. From our previous OSL experiments using the multiple and single quartz grains on the Shuangdian (SD) core in the study area (Nian et al., 2018), we found that quartz of different grain sizes had different bleaching history, and coarse silt-sized quartz generally seem to be better bleached than fine sand-sized grains. The comparison of the ages of these two quartz particle size in this study confirmed our previous findings. However, it is often difficult to extract enough fine quartz grains from sandy deposits. More cores and further research are thus needed to determine which grain-size fractions from different depositional environments represent the optimal choice for the OSL dating of samples from the paleo-incised Yangtze valley or other paleo-incised valleys around the world.

5.2. Comparison of OSL and AMS ^{14}C ages

In Fig. 7, the OSL ages are compared with their corresponding AMS ^{14}C ages. In the NT core, although the OSL and ^{14}C samples were not collected from exactly the same layer, all the quartz OSL ages were consistent with their stratigraphic order and demonstrated good agreement with their AMS ^{14}C ages, with the exception of one AMS ^{14}C sample (Beta-379322). Thus, according to the consistency of the quartz OSL ages and AMS ^{14}C ages in the NT core, we speculate that the SAR-OSL ages obtained from the 45–63 μm

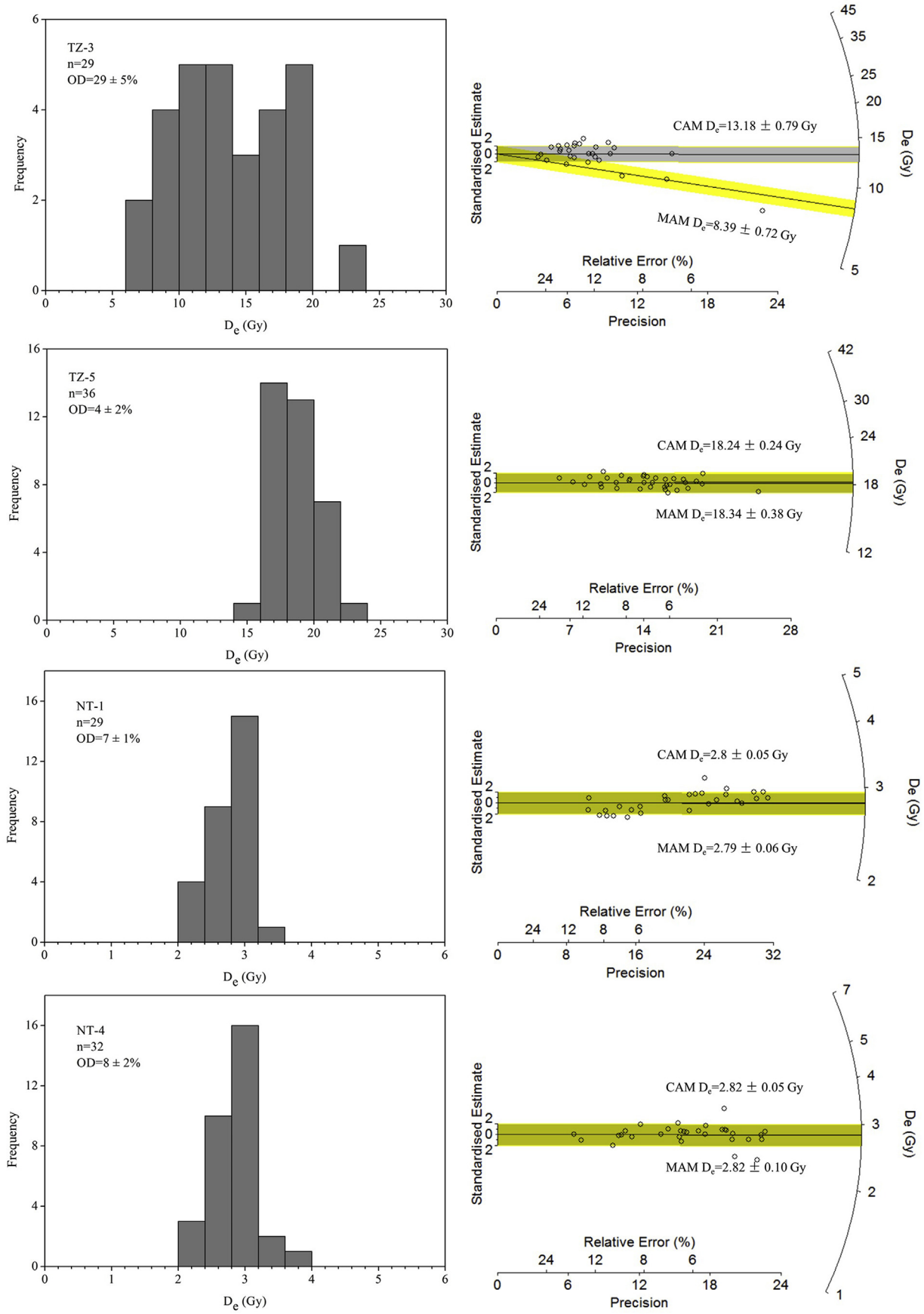

Fig. 5. Example histograms and radial plots of single-aliquot D_e distributions for the 45–63 μm quartz size fractions of samples from the TZ and NT cores. The central lines in the radial plots represent the CAM and MAM D_e values, and the corresponding shaded grey and yellow bands show the 95% confidence interval. (For interpretation of the references to color in this figure legend, the reader is referred to the Web version of this article.)

and 90–125 μm quartz size fractions represent accurate ages.

However, in the TZ core, all the ^{14}C ages using plant fragments or shells were found to be ca. 0.5–7 ka older than their corresponding quartz OSL ages. In a previous study of the Yangtze River Delta, Stanley and Chen (2000) found that two-thirds of the ^{14}C ages of Holocene deposits (i.e. mud, peat, and shell samples) are much too old (i.e. ca. 1–10 ka); they interpreted this discrepancy to be the result of the introduction of old carbon during the storage and reworking of sediments during their source-to-sink transportation pathway. Recent studies of the surface sediments from the inner continental shelf of the East China Sea, where sediments are primarily derived from the Yangtze River, have yielded ^{14}C ages of total organic carbon that are as much as 0.5 ka too old; this inconsistency is interpreted to be caused by the input of older fossil carbon during periods of peak fluvial sediment discharge (Wang and Li, 2007; Li et al., 2012). This old carbon phenomenon has also been reported in other coastal areas. Marwick et al. (2015) found that riverine particulate organic carbon arriving in the coastal zone becomes older with increasing suspended sediment load on a global scale. The AMS dating of shells is influenced by their transport and reworking in high-energy estuaries (Cearreta and Murray, 2000). The shell samples that were used for dating in our cores are often broken, thus implying that the reworking of these shells occurred under strong hydrodynamic conditions.

We found that the AMS ^{14}C ages in the TZ core are much older than those in the NT core. During the early Holocene, the Yangtze Estuary was a large, funnel-shaped estuary (Fig. 1). The tide was stronger, and flooding tides could thus transport sediment from the shelf landward to the deposition site of the TZ core. As the delta prograded towards the site of the NT core, the estuary was filled and the size of the funnel-shaped estuary became smaller. Additionally, the tides became weaker, resulting in lower flooding currents and the decreased landward transport of sediments from the shelf. This difference can explain why the shell ages in the TZ core are much older, as these ages are caused by the enhanced landward transport of reworked shelf sediments due to stronger flooding currents.

From the above data, we can find that the bottom of core TZ is much younger than that of the seaward NT core. In the former, the interval between 60 and 50 m depth belongs to estuarine deposit with an age of ca. 9–8 ka. In the NT core, the same interval is a tidal river deposit with an age of ca. 12 ka. In other words, a tidal river environment is not recorded in the TZ core. We inferred that the coring site of NT is a distributary channel within the estuary, which received minor sediment deposition until 9 ka. Similar phenomena has been found in a nearby core JD01 (northwest to the coring site), which has a sediment age ca. 6 ka for the depth between 50 and 40 m (Song et al., 2013). They interpreted that the base of core JD01 is a channel facies and the strong currents in the channel have eroded away the older sediment (Song et al., 2013).

5.3. Variations of sediment accumulation rates and implication for delta progradation

The sediment accumulation rates of the TZ and NT cores were calculated based on their quartz OSL ages (Fig. 7). In each core, a clear three-phase change in the sedimentation rate can be identified since the Holocene. In the TZ core, rapid deposition occurred at 9–8 ka, whereas a lower accumulation rate of approximately 2.3 m/ka occurred between 8 ka and 4 ka and a higher deposition rate of ca. 24 m/ka occurred between 4 ka and 3 ka. The extremely high sedimentation rate observed during the early Holocene can be linked to the occurrence of rapid sea-level rise, which created a large accommodation space for sediment infilling (Hori and Saito, 2007, Fig. 8). Following a period of rapid sea-level rise during the early Holocene, the sediment accumulation rate at the borehole drilling site decreased as a result of the landward retreat of the shoreline and the migration of the depo-center (Hori and Saito, 2007). After 8 ka, when maximum marine transgression occurs, delta begins to development in the study area, and the coastline progradates eastward. The JD01 core, which is west to the NT core, shows a rapid deposition for the upper 20 m between 6 and 5 ka (Fig. 8). The upper ca. 20 m deposit consists of delta front and delta plain facies, and the delta front facies have higher sedimentation rates than prodelta and shallow marine environments (Li et al., 2000; Hori et al., 2001, 2002). The rapid deposition rate observed between 4.5 and 3 ka is related to the development of the delta front facies at the coring site of core TZ. After 3 ka, the coring site of TZ becomes aerial and receives no further deposition due to the continuing eastward shift of coastline.

The NT core also experienced a higher sedimentation rate during the late Pleistocene and early Holocene (14–9 ka) when sea-level rise rapidly (Fig. 8). A lower accumulation rate of 2.3 m/ka occurred between 8.5 ka and 1.4 ka. Such a decline in sediment accumulation can be explained by the landward retreat of coastline during marine transgression and the subsequent delta progradation since 8 ka. Previous studies have revealed that the eastward shift of coastline to the coring site of NT occurs around 1.2 ka (Fig. 1). In other words, before 1.2 ka, the depo-center is still located west to core NT. The HQ98 core, which is west to the NT core, shows a rapid deposition between 6 and 4 ka for the upper delta front facies (Fig. 8). The JS98 core shows a rapid deposition between 3 and 1 ka for the upper delta front facies (Fig. 8). Such a migration of delta front facies is in accordance with the eastward shift history of the delta (Fig. 1). Both the NT and CM97 cores have a rapid accumulation for delta front facies around 1 ka, meaning that the top parts of both cores (ca. 20 m in length) are formed nearly at the same time period (Fig. 8).

It is noticed that the delta front facies of the westward TZ core is younger than that of the HQ98 core, which is located in a landward position. It seems contradicts with the direction of delta front progradation (Fig. 8). Similar phenomena also exist between the landward NT core and the seaward JS98 core. One possibility is that the AMS^{14}C chronology of the HQ98 and JS98 cores is overestimated according to the OSL and ^{14}C comparison in this study. Alternatively, such an inconsistency can be explained by that cores TZ and NT are located in the distributary channel while cores HQ98 and JS98 are located on the river mouth sand bar. The infilling of the distributary channel occurs later. As a result, the seaward site may become aerial earlier than the landward site.

6. Conclusions

Our results indicate that the 45–63 μm quartz grains are generally better bleached than the 90–125 μm quartz grains in the paleo-incised valley of the Yangtze River Delta. However, certain sedimentary facies yield unsatisfactory results, thus suggesting that the degree of bleaching of aqueous deposits should be properly considered when dating relatively young Holocene samples. In the landward TZ core, their adopted OSL ages yielded a coherent chronology and were consistent with their stratigraphic order, except for two samples comprising tide-influenced estuary facies that experienced rapid deposition. The AMS radiocarbon ages of the TZ core were significantly older than their corresponding OSL ages; this discrepancy is due to their reworking or contamination by old carbon material. In the seaward NT core, the adopted OSL ages obtained from both grain-size fractions are in agreement with their AMS ^{14}C ages and stratigraphic order. According to the OSL ages, both cores record temporal variations of accumulation rate. The repaid accumulation rate in early Holocene can be linked to rapid sea level rise then. The rapid deposition in the upper 20 m in both

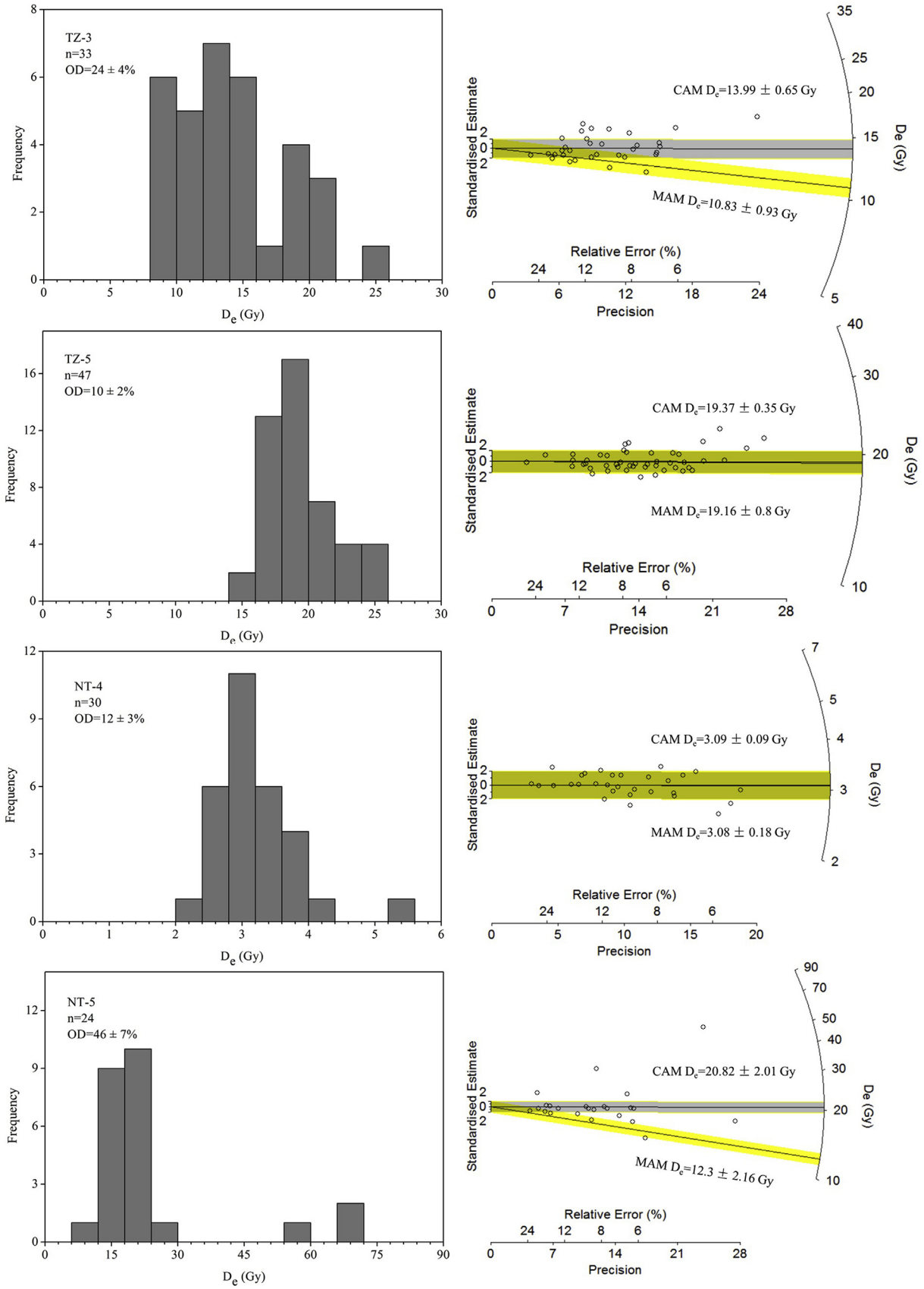

Fig. 6. Example histograms and radial plots of single-aliquot D_e distributions for the 90–125 μm quartz size fractions of samples from the TZ and NT cores. The central lines in the radial plots represent the CAM and MAM D_e values, and the corresponding shaded grey and yellow bands show the 95% confidence interval. (For interpretation of the references to color in this figure legend, the reader is referred to the Web version of this article.)

Table 3
AMS ^{14}C dating results of the samples from the TZ (Reported here) and NT cores (Bai et al., 2016).

Core ID	Lab number	Depth (m)	δ^{13}C (‰)	Material	Age		
					Uncal. BP	Cal. BP (2σ)	ka, (relative to A.D. 2013)
TZ	Beta-373527	12	−9.2	Mollusk shell	4190 ± 30	4275 ± 410	4.34 ± 0.41
	Beta-373528	21.83	−9.3		5100 ± 30	5403 ± 368	5.47 ± 0.37
	Beta-373529	23.4	−9.6		5210 ± 30	5580 ± 320	5.64 ± 0.32
	Beta-373530	24.45	−6.3	Gastropod shell	6360 ± 40	6830 ± 350	6.89 ± 0.35
	Beta-373531	26.37	−9.6	Mollusk shell	6200 ± 30	6645 ± 340	6.71 ± 0.34
	Beta-373532	30.63	−10.1		9970 ± 40	10903 ± 338	10.97 ± 0.34
	Beta-379300	38.45	−10.4		10060 ± 40	11010 ± 405	11.07 ± 0.41
	Beta-373533	38.57	−9.4		9900 ± 40	10848 ± 343	10.91 ± 0.34
	Beta-381398	59.84	−26.6	Plant fragments	8050 ± 30	8903 ± 123	8.97 ± 0.12
	Beta-381399	60.2	−11.6		8780 ± 30	9790 ± 125	9.85 ± 0.13
NT	Beta-379321	24.7	−10.3	Mollusk shell	3650 ± 30	3575 ± 370	3.64 ± 0.37
	Beta-379322	25.3	−5.8		6080 ± 30	6530 ± 320	6.59 ± 0.32
	Beta-379323	27.2	−7.8		5540 ± 30	5930 ± 315	5.99 ± 0.32
	Beta-373534	27.88	−6.2		6490 ± 30	6973 ± 328	7.04 ± 0.33
	Beta-373535	35.2	−9	Gastropod shell	7670 ± 40	8123 ± 293	8.19 ± 0.29
	Beta-373536	44.2	−5.8	Mollusk shell	8590 ± 40	9188 ± 348	9.25 ± 0.35
	Beta-373537	44.8	−8.7		8670 ± 40	9308 ± 348	9.37 ± 0.35
	Beta-383513	45.62	−27.4	Plant fragments	9420 ± 30	10650 ± 75	10.71 ± 0.08

Note: ^{14}C ages were calibrated using Calib Rev 7.1 software with the Marine13 (shell) and IntCal13 (Plant fragment) calibration curves (http://calib.qub.ac.uk/calib/).

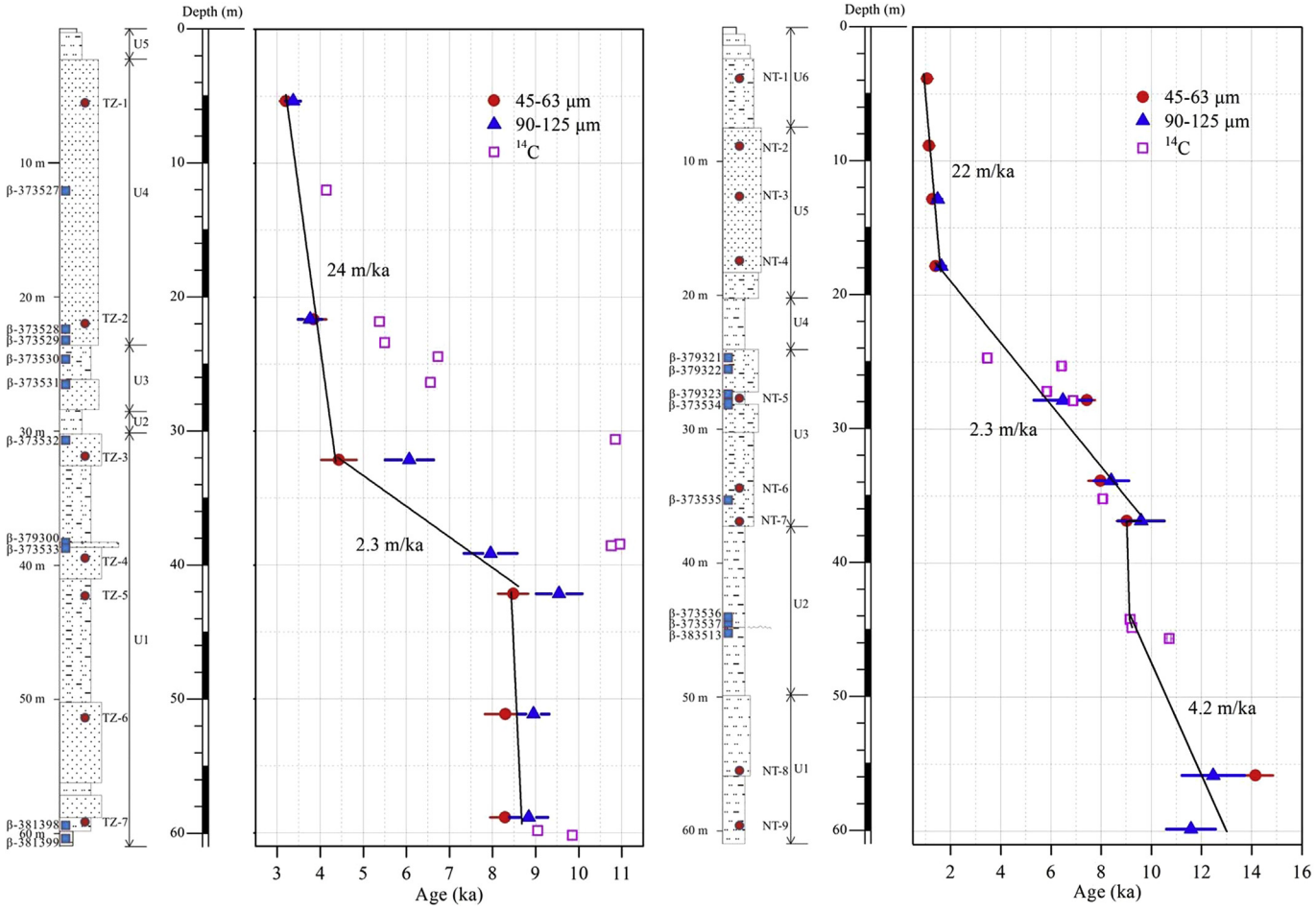

Fig. 7. Schematic profile of the TZ and NT cores showing their OSL and AMS ^{14}C ages. Circles, triangles and stars represent the ages obtained with the 45–63 μm quartz, 90–125 μm quartz and AMS ^{14}C, respectively. Accumulation rates were determined using least-squares linear regression.

cores can be linked to the delta front facies. Since delta front facies shift eastward during delta progradation, it results in that the eastward core NT has a younger age than the landward core TZ. Our results confirm that OSL dating is a promising technique in the study area.

Table 4
The OSL ages of some delta regions mentioned in the text.

Sites	No. of the core	Material	Grain size (μm)	Protocol	Age range (ka)	Well-bleached	Reference
Paleo-incised Yangtze valley	TZ; NT	Quartz	45–63 90–125	SAR	1.04–13.84	✓ ×	Reported here
Paleo-incised Yangtze valley	SD	Quartz	45–63 90–125	SAR		✓ ×	Nian et al., 2018
Yangtze River delta	ECS-DZ1 (58-0 m),	Quartz	4–11 100–200	SAR	1.3–16.6	✓ ×	Wang et al., 2015
Yangtze River delta	ECS-DZ1 (153.6–58 m),	Quartz	4–11	SAR	11.3–136	✓	Yi et al., 2014
Yellow River delta	LZ908; BH1; BH2	Quartz	4-11; 38–63; 63–90; 90-125	SAR; MAR[a]	0.42–144	✓	Yi et al., 2013
South Yellow Sea	YZ07	Quartz	90–200	SAR	1.9–51.3	✓	Gao et al., 2016
South Yellow Sea	YZ07	Quartz	4-11; 90–200	SAR SAR; post-IR OSL; pulsed OSL	0.13–10.84	✓ √[b]	Gao et al., 2017
Yangtze subaqueous delta	YD13-G3; H1	Quartz polymineral	4–11 4–11	SAR pIRIR[c]	1.92–6.77	✓ ✓	Sugisaki et al., 2015
Southern Yangtze delta Plain	QP88; WJ	Quartz	4–11	SAR	27–100	✓	Wang et al., 2013b
Mississippi delta	WLDI	Quartz	4-11; 75-180	SAR	0.024–0.333	√[d]	Shen and Mauz, 2012
Mississippi Delta (Bayou Lafourche)	13 cores sites at Paincourtville, Napoleonville and Elmfield	Quartz	4-11; 75–125; 75–180; 90–180; 100-200	SAR	0.63–5.89	✓	Shen et al., 2015
Mekong River delta	Beach ridges of Tra Vinh, South/Central/North Ben Tre, Cai Lay, and Tien Giang	Quartz	125–180	SAR	0.04–5.57	✓	Tamura et al., 2012
Ganges-Brahmaputra-Meghna Delta	NCL-1116002-014	Quartz polymineral	4-11; 11-20 75-125; 180-250 4-11; 11-20	SAR SAR MS-SAR	0–0.4	✓ × ×	Chamberlain et al., 2017
Nakdong delta	ND 01	Quartz	4-11; 90-212	SAR	0.4–29.4	✓	Kim et al., 2015

[a] MAR: Multiple-aliquot regenerative-dose protocol.
[b] Some samples have the problem of age underestimation (feldspar contamination), and post-IR or pulsed OSL dating techniques can overcome the problem.
[c] pIRIR: post-IR IRSL SAR protocol.
[d] Quartz was bleached to a very small residual level (ca. 100 a on average for both sandy and fine silt-sized quartz).

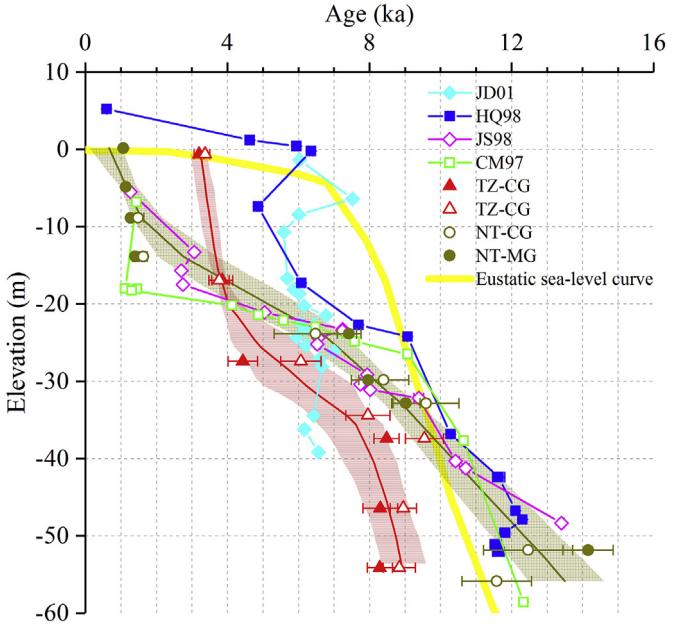

Fig. 8. Age-depth relationships and accumulation curves for cores (TZ and NT) in this study and previous studies (HQ98, JS98 and CM97, Hori et al., 2001, 2002; JD01, Song et al., 2013) and eustatic sea-level curve (Lambeck et al., 2014). Bacon age-depth models of cores TZ and NT were presented (Blaauw and Christen, 2011). The areas filled by the horizontal (TZ) and crossing (NT) lines show the model's 95% probability interval and the central lines represent the single 'best' age-depth model. The weighted mean value of the paired data (two grain-size fractions, in Table 2) was used for age-depth model construction.

Acknowledgements

We thank anonymous reviewers for insightful readings and constructive suggestions that have greatly improved the clarity of the paper. This research has been supported by the National Natural Science Foundation of China (41771009; 41271223; 41302135), the China Postdoctoral Special Science Foundation (2017T100284), the China Postdoctoral Science Foundation (2015M571521), and the State Key Laboratory Special Fund (2014RCDW02, SKLEC-2012KYYW01).

Appendix A. Supplementary data

Supplementary data related to this article can be found at https://doi.org/10.1016/j.quaint.2018.01.011.

References

Arnold, L.J., Bailey, R.M., Tucker, G.E., 2007. Statistical treatment of fluvial dose distributions from southern Colorado arroyo deposits. Quat. Geochronol. 2, 162–167.
Arnold, L.J., Roberts, R.G., 2009. Stochastic modelling of multi-grain equivalent dose (D_e) distributions: implications for OSL dating of sediment mixtures. Quat. Geochronol. 4, 204–230.
Bai, X.X., Zhang, W.G., Dong, Y., Pan, D.D., Wang, Z.H., Sun, Q.L., Chen, J., Chen, Z.Y., Liu, J.Y., 2016. Magnetic properties of Holocene tidal flats in the Yangtze Delta and their Paleoenvironmental implications. Acta Sedimentol. Sin. 34, 1165–1175 (In Chinese with English abstract).
Ballarini, M., Wallinga, J., Wintle, A.G., Bos, A.J.J., 2007. A modified SAR protocol for optical dating of individual grains from young quartz samples. Radiat. Meas. 42, 360–369.
Bateman, M.D., 2015. The application of luminescence dating in sea-level studies. In: Shennan, I., Long, A.J., Horton, B.P. (Eds.), Handbook of Sea-level Research, vol. 27, pp. 404–417. Chapter.

Blaauw, M., Christen, J.A., 2011. Flexible paleoclimate age-depth models using an autoregressive gamma process. Behav. Anal. 6, 457–474.
Bøtter-Jensen, L., Andersen, C.E., Duller, G.A.T., Murray, A.S., 2003. Developments in radiation, stimulation and observation facilities in luminescence measurements. Radiat. Meas. 37, 535–541.
Brennan, B.J., Lyons, R.G., Phillips, S.W., 1991. Attenuation of alpha particle track dose for spherical grains. International Journal of Radiation Applications and Instrumentation. Part D. Nucl. Tracks Radiat. Meas. 18, 249–253.
Cearreta, A., Murray, J.W., 2000. AMS ^{14}C dating of Holocene estuarine deposits: consequences of high-energy and reworked foraminifera. Holocene 10, 155–1159.
Chamberlain, E.L., Wallinga, J., Reimann, T., Goodbred Jr., S.L., Steckler, M.S., Shen, Z.X., Sincavage, R., 2017. Luminescence dating of delta sediments: Novel approaches explored for the Ganges-Brahmaputra-Meghna Delta. Quat. Geochronol. 41, 97–111.
Delta Research Group, Department of Marine Geology, Tongji University, 1978. Holocene formation and development of the Yangtze Delta. Chin. Sci. Bull. 35, 310–313 (In Chinese).
Duller, G.A.T., 2003. Distinguishing quartz and feldspar in single grain luminescence measurements. Radiat. Meas. 37, 161–165.
Durcan, J.A., King, G.E., Duller, G.A.T., 2015. DRAC: Dose rate and age calculation for trapped charge dating. Quat. Geochronol. 28, 54–61.
Feng, Z.B., Liu, B.H., Zhao, Y.X., Li, X.S., Jiang, L., Si, S.K., 2016. Spatial and temporal variations and controlling factors of sediment accumulation in the Yangtze River estuary and its adjacent sea area in the Holocene, especially in the Early Holocene. Continent. Shelf Res. 125, 1–17.
Galbraith, R.F., Roberts, R.G., Laslett, G.M., Yoshida, H., Olley, J.M., 1999. Optical dating of single and multiple grains of quartz from Jinmium rock shelter, Northern Australia: part 1, experimental details and statistical models. Archaeometry 41, 339–364.
Gao, L., Long, H., Shen, J., Yu, G., Yin, Y., 2016. High-resolution OSL dating of a coastal sediment sequence from the South Yellow Sea. Geochronometria 43, 143–154.
Gao, L., Long, H., Shen, J., Yu, G., Yin, Y., 2017. Optical dating of Holocene tidal deposits from the southwestern coast of the South Yellow Sea using different grain-size quartz fractions. J. Asian Earth Sci. 135, 155–165.
Guerin, G., Mercier, N., Nathan, R., Adamiec, C., Lefrais, Y., 2012. On the use of the infinite matrix assumption and associated concepts: a critical review. Radiat. Meas. 47, 778–785.
Hori, K., Saito, Y., 2007. An early Holocene sea-level jump and delta initiation. Geophys. Res. Lett. 34, L18401.
Hori, K., Saito, Y., Zhao, Q.H., Cheng, X.R., Wang, P.X., Sato, Y., Li, C.X., 2001. Sedimentary facies of the tide-dominated paleo-Changjiang (Yangtze) estuary during the last transgression. Mar. Geol. 177, 331–351.
Hori, K., Saito, Y., Zhao, Q.H., Wang, P.X., 2002. Evolution of the coastal depositional systems of the Changjiang (Yangtze) River in response to late Pleistocene-Holocene sea-level changes. J. Sediment. Res. 72, 884–897.
Jacobs, Z., 2008. Luminescence chronologies for coastal and marine sediments. Boreas 37, 508–535.
Kim, J.C., Cheong, D., Shin, S., Park, Y.H., Hong, S.S., 2015. OSL chronology and accumulation rate of the Nakdong deltaic sediments, southeastern Korean Peninsula. Quat. Geochronol. 30, 245–250.
Kong, G.,S., Lee, C.W., 2005. Marine reservoir corrections (ΔR) for southern coastal waters of Korea. The Sea, Journal of the Korean Society of Oceanography 10, 124–128.
Lambeck, K., Rouby, H., Purcell, A., Sun, Y.Y., Sambridge, M., 2014. Sea level and global ice volumes from the last glacial maximum to the Holocene. Proceedings of the National Academy of Sciences of the United States of America 15296–15303.
Lamothe, M., 2016. Luminescence dating of interglacial coastal depositional systems: recent developments and future avenues of research. Quat. Sci. Rev. 146, 1–27.
Li, C.X., Chen, Q.Q., Zhang, J.Q., Yang, S.Y., Fan, D.D., 2000. Stratigraphy and paleoenvironmental changes in the Yangtze delta during late Quaternary. J. Asian Earth Sci. 18, 453–469.
Li, S.H., Sun, J.M., Zhao, H., 2002. Optical dating of dune sands in the northeastern deserts of China. Palaeogeogr. Palaeoclimatol. Palaeoecol. 181, 419–429.
Li, X.X., Bianchi, T.S., Allison, M.A., Chapman, P., Mitra, S., Zhang, Z.R., Yang, G.P., Yu, Z.G., 2012. Composition, abundance and age of total organic carbon in surface sediments from the inner shelf of the East China Sea. Mar. Chem. 145–147, 37–52.
Marwick, T.R., Tamooh, F., Teodoru, C.R., Borges, A.V., Darchambeau, F., Bouillon, S., 2015. The age of river-transported carbon: a global perspective. Global Biogeochem. Cycles 29, 122–137.
Murray, A.S., Wintle, A.G., 2000. Luminescence dating of quartz using an improved single-aliquot regenerative-dose protocol. Radiat. Meas. 32, 57–73.
Murray, A.S., Wintle, A.G., 2003. The single aliquot regenerative dose protocol: potential for improvements in reliability. Radiat. Meas. 37, 377–381.
Nian, X.M., Zhang, W.G., Wang, Z.H., Sun, Q.L., Chen, J., Chen, Z.Y., 2018. The chronology of a sediment core from incised valley of the Yangtze River delta: comparative OSL and AMS ^{14}C dating. Mar. Geol. 395, 320–330.
Oliver, T.S., Dougherty, A.J., Gliganic, L.A., Woodroffe, C.D., 2015. Towards more robust chronologies of coastal progradation: optically stimulated luminescence ages for the coastal plain at Moruya, south-eastern Australia. Holocene 25, 536–546.
Rees-Jones, J., 1995. Optical dating of young sediments using fine-grain quartz. Ancient TL 13, 9–14.
Reimer, P.J., Bard, E., Bayliss, A., Beck, J.W., Blackwell, P.G., Bronk Ramsey, C., Buck, C.E., Cheng, H., Edwards, R.L., Friedrich, M., Grootes, P.M., Guilderson, T.P., Haflidason, H., Hajdas, I., Hatté, C., Heaton, T.J., Hoffman, D.L., Hogg, A.G., Hughen, K.A., Kaiser, K.F., Kromer, B., Manning, S.W., Niu, M., Reimer, R.W., Richards, D.A., Scott, E.M., Southon, J.R., Staff, R.A., Turney, C.S.M., van der Plicht, J., 2013. IntCal13 and Marine13 radiocarbon age calibration curves 0–50,000 years cal BP. Radiocarbon 55, 1869–1887.
Roberts, H.M., Plater, A.J., 2007. Reconstruction of Holocene foreland progradation using optically stimulated luminescence (OSL) dating: an example from Dungeness, UK. Holocene 17, 495–505.
Shen, Z.X., Mauz, B., 2012. Optical dating of young deltaic deposits on a decadal time scale. Quat. Geochronol. 10, 110–116.
Shen, Z.X., Törnqvist, T.E., Mauz, B., Chamberlain, E.L., Nijhuis, A.G., Sandoval, L., 2015. Episodic overbank deposition as a dominant mechanism of floodplain and delta-plain aggradation. Geology 43, 875–878.
Song, B., Li, Z., Saito, Y., Okuno, J., Li, Z., Lu, A.Q., Hua, D., Li, J., Li, Y.X., Nakashima, R., 2013. Initiation of the Changjiang (Yangtze) delta and its response to the mid-Holocene sea level change. Palaeogeograp. Palaeoclimatol. Palaeoecol. 388, 81–97.
Southon, J., Kashgarian, M., Fontugne, M., Metivier, B., Yim, W.W.-S., 2002. Marine reservoir corrections for the indian Ocean and Southeast Asia. Radiocarbon 44, 167–180.
Stanley, D.J., Chen, Z.Y., 2000. Radiocarbon Dates in China's Holocene Yangtze Delta: record of sediment storage and reworking, not timing of Deposition. J. Coast Res. 16, 1126–1132.
Sugisaki, S., Buylaert, J.P., Murray, A.S., Tada, R., Zheng, H.B., Ke, W., Saito, K., Chao, L., Li, S.Y., Irino, T., 2015. OSL dating of fine-grained quartz from Holocene Yangtze delta sediments. Quat. Geochronol. 30, 226–232.
Tamura, T., Saito, Y., Nguyen, V.L., Ta, T.K.O., Bateman, M.D., Matsumoto, D., Yamashita, S., 2012. Origin and evolution of interdistributary delta plains; insights from Mekong River delta. Geology 40, 303–306.
Wang, J.T., Guo, X.M., Xu, S.Y., Li, P., Li, C.X., 1981. Evolution of the Holocene changjiang Delta. Acta Geol. Sin. 55, 67–81 (In Chinese with English abstract).
Wang, X.C., Li, A.C., 2007. Preservation of black carbon in the shelf sediments of the East China Sea. Chin. Sci. Bull. 52, 3155–3161.
Wang, Y., Long, H., Yi, L., Yang, L.H., Ye, X.Y., Shen, J., 2015. OSL chronology of a sedimentary sequence from the inner-shelf of the East China Sea and its implication on post-glacial deposition history. Quat. Geochronol. 30, 282–287.
Wang, Z.H., Jones, B.G., Chen, T., Zhao, B.C., Zhan, Q., 2013b. A raised OIS 3 sea level recorded in coastal sediments, southern Changjiang delta plain, China. Quat. Res. 79, 424–438.
Wang, Z.H., Zhan, Q., Long, H.Y., Saito, Y., Gao, X.Q., Wu, X.X., Li, L., Zhao, Y.N., 2013a. Early to mid-Holocene rapid sea-level rise and coastal response on the southern Yangtze delta plain, China. J. Quat. Sci. 28, 659–672.
Wang, Z.H., Zhuang, C.C., Saito, Y., Chen, J., Zhan, Q., Wang, X.D., 2012. Early mid-Holocene sea-level change and coastal environmental response on the southern Yangtze delta plain, China: implications for the rise of Neolithic culture. Quat. Sci. Rev. 35, 51–62.
Wallinga, J., 2002. Optically stimulated luminescence dating of fluvial deposits: a review. Boreas 31, 303–322.
Xu, K.H., Li, A.C., Liu, J.P., Milliman, J.D., Yang, Z.S., Liu, C.S., Kao, S.J., Wan, S.M., Xu, F.J., 2012. Provenance, structure, and formation of the mud wedge along inner continental shelf of the East China Sea: a synthesis of the Yangtze dispersal system. Mar. Geol. 291–294, 176–191.
Yi, L., Lai, Z.P., Yu, H.J., Xu, X.Y., Su, Q., Yao, J., Wang, X.L., Shi, X.F., 2013. Chronologies of sedimentary changes in the south Bohai Sea, China: constraints from luminescence and radiocarbon dating. Boreas 42, 267–284.
Yi, L., Ye, X.Y., Chen, J.B., Li, Y., Long, H., Wang, X.L., Du, J.H., Zhao, S.L., Deng, C.L., 2014. Magnetostratigraphy and luminescence dating on a sedimentary sequence from northern East China Sea: constraints on evolutionary history of eastern marginal seas of China since the Early Pleistocene. Quat. Int. 349, 316–326.
Yoneda, M., Uno, H., Shibata, Y., Suzuki, R., Kumamoto, Y., Yoshida, K., Sasaki, T., Suzuki, A., Kawahata, H., 2007. Radiocarbon marine reservoir ages in the western Pacific estimated by pre-bomb molluscan shells. Nucl. Instrum. Meth. Phys. Res. B 259, 432–437.
Zhang, X., Dalrymple, R.W., Lin, C.M., 2017. Facies and stratigraphic architecture of the late Pleistocene to early Holocene tide-dominated paleo-Changjiang (Yangtze River) delta. Geol. Soc. Am. Bull. https://doi.org/10.1130/B31663.1.